FRONTIERS OF PHYSICS

RESEARCH ARTICLE
Volume 21 / Issue 11 / 115203 / 2026

Interlayer sliding modulation of spin Hall and spin Nernst effects in two-dimensional altermagnets

Siyuan Liu[1], Ling Bai[1], Xiangju Wang[1], Libor Šmejkal[2,3], Jairo Sinova[4], Yuriy Mokrousov[4,5], Gui-Bin Liu[1,†], Wanxiang Feng[1,‡]

1 Key Lab of Advanced Optoelectronic Quantum Architecture and Measurement (MOE),
Beijing Key Lab of Nanophotonics & Ultrafine Optoelectronic Systems, and School of Physics,
Beijing Institute of Technology, Beijing 100081, China
2 Max Planck Institute for the Physics of Complex Systems, Nöthnitzer Str. 38, 01187 Dresden, Germany
3 Institute of Physics, Czech Academy of Sciences, Cukrovarnická 10, 162 00 Praha 6, Czech Republic
4 Institute of Physics, Johannes Gutenberg University Mainz, Staudingerweg 7, 55128 Mainz, Germany
5 Peter Grünberg Institute (PGI-1), Forschungszentrum Jülich and JARA, 52425 Jülich, Germany
Corresponding authors. E-mail: †gbliu@bit.edu.cn, ‡wxfeng@bit.edu.cn

Received December 8, 2025; accepted March 2, 2026

ABSTRACT

Altermagnets constitute a recently identified magnetic phase that combines the absence of macroscopic magnetization, characteristic of antiferromagnets, with the spin splitting typically associated with ferromagnets. This hybrid nature enables stray-field-free spin transport and ultrafast spin dynamics, offering new opportunities for dissipationless spintronics and spin-caloritronics. Here, we perform a comprehensive symmetry analysis and advanced first-principles calculations to investigate the intrinsic spin Hall and spin Nernst effects in two-dimensional altermagnets, using bilayer $\mathrm{MnPSe_3}$ as a representative example. In the nonrelativistic limit, interlayer sliding induces a *d*-wave-like spin splitting and generates time-reversal-odd, intraband-dominated spin Hall and spin Nernst responses. Changing the sliding direction alters the associated symmetry operations, thereby modifying the spin splitting of the Fermi surface and enabling tunable control of spin-transport properties. This modulation originates from symmetry-driven variations in the relative contributions of opposite spins. Our findings identify interlayer sliding as an effective route to tuning spin transport in altermagnets, establishing a versatile two-dimensional platform for exploring the interplay between altermagnetism and spin transport, and paving the way for future advances in altermagnetic spintronics and spin-caloritronics.

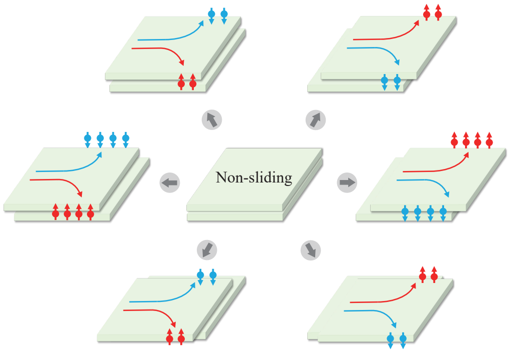

Keywords altermagnet, spin Hall effect, spin Nernst effect, two-dimensional system

1 Introduction

Spintronics aims to exploit the interplay between spin and charge degrees of freedom to manipulate both equilibrium and nonequilibrium phenomena in materials and devices. Among its core objectives, the generation, detection, and control of transverse spin currents are of central importance [1]. A transverse spin current induced by a longitudinal electric field is known as the

---

*Special Topic: Altermagnets: Exploring New Physical Phenomena and Effects (Editor: Sandong Guo).

https://doi.org/10.15302/frontphys.2026.115203

spin Hall effect (SHE) [2], which serves as a fundamental mechanism for creating and detecting spin currents. Analogously, a longitudinal temperature gradient can also drive a transverse spin current, giving rise to the spin Nernst effect (SNE). In both cases, the transverse spin response originates from two distinct mechanisms: extrinsic contributions — such as side-jump and skew-scattering processes — which strongly depend on carrier–impurity interactions [3, 4]; and intrinsic contributions, which arise purely from the electronic structure of a perfect crystal and are closely tied to band topology [5, 6].

From the perspective of time-reversal symmetry (T), the intrinsic SHE can be decomposed into T-even and T-odd components [7]. The T-even contribution originates from spin Berry curvature induced by spin-orbit-coupling (SOC) [5, 6] and has been extensively explored in both magnetic [7–9] and nonmagnetic systems [10–14]. By contrast, the T-odd contribution depends sensitively on the detailed electronic band structure and does not rely on the strength of SOC. This provides a promising mechanism for generating and tuning spin currents in materials composed of light elements, where SOC is intrinsically weak. Despite these advantages, studies on the T-odd SHE remain limited. It is further believed to vanish in conventional collinear compensated magnetic systems due to the absence of essential spin splitting, which has imposed significant constraints on both fundamental understanding and practical development of spintronic functionalities.

Recently, a newly identified class of magnets — termed altermagnets (AMs) [15, 16] — has attracted considerable attention due to their promising potential in spintronic applications [17]. In AMs, magnetic sublattices with opposite spin orientations are connected by rotational or mirror symmetries, in contrast to conventional collinear antiferromagnets, where they are related through inversion or translational symmetries. These symmetry operations enforce alternating spin splittings across the electronic band structure, giving rise to a wide array of unconventional physical phenomena [18–34]. Among these, the emergence of an intrinsic T-odd SHE is particularly notable, as it resolves the long-standing belief that such an effect is forbidden in collinear compensated magnetic systems [35], thereby expanding the pool of viable material platforms for spintronics. For instance, in altermagnetic $\mathrm{RuO_2}$, the corresponding transverse spin conductivity exceeds by a factor of three the record values reported in nonmagnetic materials and exhibits strong sensitivity to spin orientation. Despite these promising attributes, progress in exploiting AMs for generating and modulating T-odd SHE has been limited, particularly in two-dimensional (2D) systems. Moreover, it is essential to identify control mechanisms beyond spin reorientation to meet the demands of high-performance and device-compatible functionalities.

In this work, through comprehensive symmetry analysis and advanced first-principles calculations, we systematically investigate how interlayer sliding modulates the intrinsic SHE and SNE in 2D bilayer altermagnets, using $\mathrm{MnPSe_3}$ as a representative example. In the nonrelativistic limit, interlayer sliding induces a d-wave–like spin splitting in momentum space, whose pattern depends sensitively on the sliding direction and its associated symmetry operations. By varying the sliding direction, $\mathrm{MnPSe_3}$ exhibits pronounced orientation-dependent spin splitting. Based on spin and magnetic group analyses, we further determine the symmetry constraints on the spin Hall conductivity (SHC) and spin Nernst conductivity (SNC) tensors in both nonrelativistic and relativistic cases. Our calculations reveal that the T-odd intraband contribution dominates the SHE and SNE. More importantly, both the sign and magnitude of the SHC and SNC can be efficiently tuned by adjusting the sliding direction, and this sliding-induced modulation remains robust with or without SOC. These findings not only establish interlayer sliding as an effective route for controlling spin-transport properties but also highlight bilayer $\mathrm{MnPSe_3}$ as a compelling 2D platform for exploring the interplay between altermagnetism and spin transport, paving the way for advances in altermagnetic spintronics and spin-caloritronics.

2 Theory and computational details

Under an applied electric field E along the j direction, the linear response of a spin current flowing in the i direction and polarized along the s direction ($i, j, s \in \{x, y, z\}$) is given by

$$\mathcal{J}_i^{E,s} = \sigma_{ij}^s E_j, \tag{1}$$

where σ_{ij}^s denotes the SHC. According to its behavior under T, the SHC can be decomposed into two parts as [7]

$$\sigma_{ij}^s = \sigma_{ij}^{s,\text{odd}} + \sigma_{ij}^{s,\text{even}}, \tag{2}$$

with

$$\sigma_{ij}^{s,\text{odd}} = \frac{\hbar^2\Gamma}{V} \sum_{n,m,\boldsymbol{k}} \frac{f_{mk} - f_{nk}}{\varepsilon_{nk} - \varepsilon_{mk}} \frac{\mathrm{Re}\Big(\langle n|J_{\boldsymbol{k},i}^s|m\rangle\langle m|J_{\boldsymbol{k},j}|n\rangle\Big)}{(\varepsilon_{nk} - \varepsilon_{mk})^2 + (\hbar\Gamma)^2}, \tag{3}$$

$$\sigma_{ij}^{s,\text{even}} = -\frac{\hbar}{V} \sum_{n,m,\boldsymbol{k}} (f_{mk} - f_{nk}) \frac{\mathrm{Im}\Big(\langle n|J_{\boldsymbol{k},i}^s|m\rangle\langle m|J_{\boldsymbol{k},j}|n\rangle\Big)}{(\varepsilon_{nk} - \varepsilon_{mk})^2 + (\hbar\Gamma)^2}. \tag{4}$$

Here, V is the volume and $f_{nk} = \left[\mathrm{e}^{(\varepsilon_{nk}-\varepsilon_F)/(k_B\mathcal{T})} + 1\right]^{-1}$ is the Fermi–Dirac distribution with Fermi energy ε_F. The current kernels are defined as $J^s_{\boldsymbol{k},i} = \frac{1}{2}e\left(\hat{\mathcal{S}}_s v_{\boldsymbol{k},i} + v_{\boldsymbol{k},i}\hat{\mathcal{S}}_s\right)$ and $J_{\boldsymbol{k},j} = ev_{\boldsymbol{k},j}$, where e is the elementary charge, $\hat{\mathcal{S}}_s$ is the spin operator polarized along direction s, and $v_{\boldsymbol{k},i/j}$ is the velocity operator along direction i/j. The summand of $\sigma_{ij}^{s,\text{odd(even)}}$ with respect to the band indices is denoted as $D_{ij}^{s,\text{odd(even)}}(\boldsymbol{k})$. Furthermore, $\sigma_{ij}^{s,\text{odd}}$ can be decomposed into an intraband contribution $\sigma_{ij}^{s,\text{odd-intra}}$ $(m = n)$ and an interband contribution $\sigma_{ij}^{s,\text{odd-inter}}$ $(m \neq n)$.

In Eqs. (3) and (4), $\Gamma = 1/\tau$ is an artificial spectral broadening parameter, where the relaxation time τ can be estimated using the semiclassical relation [36, 37]

$$\tau = \mu m^*/e. \tag{5}$$

Here, μ and m^* denote the carrier mobility and the effective mass, respectively. Within the framework of deformation potential theory, μ can be evaluated, allowing τ to be expressed as [38, 39]

$$\tau = \frac{\hbar^3 C_{2D}}{k_B \mathcal{T} m_d E_1^2}, \tag{6}$$

where C_{2D} is the in-plane elastic modulus, k_B is the Boltzmann constant, and $\mathcal{T}$ is the temperature. The quantity $m_d = \sqrt{m_x^* m_y^*}$ is the average effective mass, with m_x^* and m_y^* denoting the effective masses along the x and y directions, respectively. The deformation potential constant E_1 is defined as $E_1 = \frac{\mathrm{d}E_\text{edge}}{\mathrm{d}u}$, where E_edge is the energy of the conduction- or valence-band edge and u represents the applied uniaxial strain.

Similarly, a temperature gradient $\nabla\mathcal{T}$ can play the role analogous to that of an applied electric field E, driving transverse spin current through the sample. This thermal response, known as the SNE, can be expressed as

$$\mathcal{J}_i^{\nabla T,s} = \alpha_{ij}^s \nabla\mathcal{T}_j, \tag{7}$$

where α_{ij}^s denotes the SNC. According to the generalized Landauer–Büttiker formalism [40–42], the SNC is related to the SHC through

$$\alpha_{ij}^s = \int_{-\infty}^{\infty} (\varepsilon - \varepsilon_F)\left(-\frac{\partial f}{\partial\varepsilon}\right)\sigma_{ij}^s(\varepsilon)\mathrm{d}\varepsilon. \tag{8}$$

Under an applied electric field E along the j direction $(j \in x, y, z)$, the linear response of a charge current flowing in the same direction is given by

$$\mathcal{J}_j^E = \sigma_{jj} E_j, \tag{9}$$

where σ_{jj} denotes the longitudinal charge conductivity. Within the semiclassical Boltzmann transport formalism [43], σ_{jj} can be written as [43–45]

$$\sigma_{jj} = e^2 \int_{-\infty}^{+\infty} \left(-\frac{\partial f}{\partial\varepsilon}\right)\Sigma_{jj}(\varepsilon)\mathrm{d}\varepsilon. \tag{10}$$

Here, the $\Sigma_{jj}(\varepsilon)$ is the transport distribution function, defined as

$$\Sigma_{jj}(\varepsilon) = \frac{\tau}{V}\sum_{n,\boldsymbol{k}} v_{\boldsymbol{k},j}^2 \delta(\varepsilon - \varepsilon_{nk}), \tag{11}$$

where the constant relaxation-time approximation is adopted and $\delta(\varepsilon - \varepsilon_{nk})$ represents the Dirac delta function.

The electronic structures were calculated using the Vienna *ab initio* simulation package (VASP) [46, 47], within the framework of density functional theory (DFT). The generalized gradient approximation (GGA) with the Perdew–Burke–Ernzerhof (PBE) parameterization [48] was employed to describe electron–electron exchange-correlation effects, while the projected augmented-wave (PAW) method [49] was used to account for electron–ion interactions. An energy cutoff of 500 eV was used for the plane-wave basis, along with a uniform k-mesh of 9 × 9 × 1 for 2D system. The self-consistent field calculations were considered converged when the total energy change was below 1×10^{-6} eV and the residual forces on atoms were less than 1×10^{-2} eV/Å. To properly describe the localization of Mn $3d$ orbitals, a Hubbard correction of $U_\text{eff} = 5$ eV was applied using the Dudarev scheme [50]. Long-range van der Waals interactions were included via the semiempirical DFT-D3 method [51]. A vacuum region of more than 15 Å was added along the out-of-plane direction to avoid spurious interactions between adjacent slabs. After obtaining converged ground-state charge densities, maximally localized Wannier functions were constructed using the Wannier90 package [52], incorporating the p orbitals of Se and the d orbitals of Mn atoms. The spin- and charge-transport properties were evaluated using an *ab initio* tight-binding Hamiltonian constructed from maximally localized Wannier functions. The transverse components were computed using our in-house developed codes, whereas the longitudinal components were obtained with the BoltzWann package [45]. To achieve well-converged transport results, we employed an ultra-dense k-mesh of at least $700 \times 700 \times 1$.

3 Results and discussion

For collinear AMs, the nonrelativistic spin-split band structures can be systematically characterized within the framework of spin group theory. A spin point group $\mathbb{S}$ can be constructed from a crystallographic point group $\mathbb{G}$ through the relation [13–17, 32]

$$\mathbb{S} = [E||\mathbb{H}] + [C_2||\mathbb{G} - \mathbb{H}], \tag{12}$$

where $[\mathcal{R}_s||\mathcal{R}_l]$ denotes a combined symmetry operation consisting of $\mathcal{R}_s$ acting in spin space and $\mathcal{R}_l$ in real space. Here, E is the identity operation in spin space, C_2 is a twofold rotation perpendicular to the collinear spin

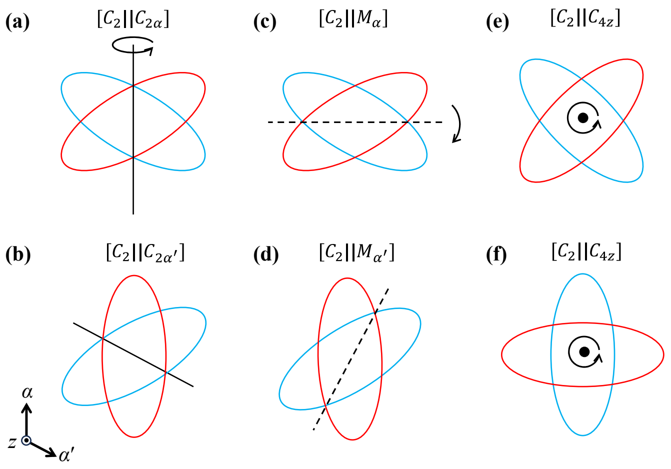

Fig. 1 Schematic illustration of the orientation-dependent spin splitting induced by spin-group symmetries: **(a)** $[C_2||C_{2\alpha}]$, **(b)** $[C_2||C_{2\alpha'}]$, **(c)** $[C_2||M_\alpha]$, **(d)** $[C_2||M_{\alpha'}]$, and **(e, f)** $[C_2||C_{4z}]$. Red and blue lines represent bands with opposite spin polarizations. The solid lines indicate the in-plane rotation axes of $C_{2\alpha}$ and $C_{2\alpha'}$, while the dashed lines denote the mirror planes M_α and $M_{\alpha'}$.

axis, and $\mathbb{H}$ is a halving subgroup of $\mathbb{G}$. The term $[E||\mathbb{H}]$ preserves the spin orientation and operates within same-spin sublattices, whereas $[C_2||\mathbb{G}-\mathbb{H}]$ relates sublattices with opposite spin orientations.

For the 2D case, the spatial operations appearing in $[C_2||\mathbb{G}-\mathbb{H}]$ must exclude inversion P, mirror M_z, and the twofold rotation C_{2z} (with the z axis perpendicular to the atomic plane), as these symmetries enforce spin degeneracy of the electronic bands, i.e., $E(\boldsymbol{k},s)=E(\boldsymbol{k},-s)$, where $\boldsymbol{k}$ and s denote momentum and spin indices, respectively [32]. The remaining admissible operations include the fourfold rotation C_{4z}, in-plane twofold rotations $C_{2\alpha}$, and vertical mirrors M_α, where α specifies an arbitrary in-plane direction. When combined with the spin-space rotation C_2, all three classes of operations can induce anisotropic spin splitting in the band structure [see Fig. 1]. For $[C_2||C_{2\alpha}]$ and $[C_2||M_\alpha]$, varying the in-plane axis α — for example, rotating it to a new direction α' — causes the corresponding band structure to evolve accordingly [see Figs. 1(a)–(d)]. This pronounced directional dependence enables effective tuning of nonrelativistic band structures by controlling the orientation of the underlying symmetries. In contrast, although the $[C_2||C_{4z}]$ symmetry can also induce spin splitting, its directional character cannot be regulated in 2D systems, because multiple distinct spin-splitting patterns correspond to the same symmetry operation [see Figs. 1(e) and (f)]. Therefore, $[C_2||C_{4z}]$ is unsuitable for symmetry-based tuning of nonrelativistic band structures in 2D AMs.

For 2D van der Waals layered materials, the orientation of symmetry operations can be readily and effectively controlled via interlayer sliding. Monolayer $\mathrm{MnPSe_3}$ exhibits an antiferromagnetic ground state with an in-plane easy axis and a Néel temperature of approximately 40 K [53]. As illustrated in Fig. 2, in the absence of SOC, stacking two $\mathrm{MnPSe_3}$ monolayers in a configuration that preserves the combined symmetry $[C_2||M_z]$ yields a bilayer type-IV collinear magnet [32] that exhibits robust magnetoelectric coupling [54]. The corresponding crystallographic point group is $\mathbb{G}=D_{3h}$, and the halving subgroup can be chosen as $\mathbb{H}=D_3$. The bilayer $\mathrm{MnPSe_3}$ thus retains the following spin point group symmetry operations: $[E||E]$, $[E||C_{3z}^{\pm}]$, $[E||C_{2\alpha}]$ with $\alpha=[100],[010],[110]$, $[C_2||M_z]$, $[C_2||PC_{6z}^{\pm}]$, and $[C_2||M_\alpha]$ with $\alpha=[210],[120],[1\bar{1}0]$. Among these, the operation $[C_2||M_z]$ enforces spin degeneracy, as shown in the central part of Fig. 2. This bilayer type-IV magnet turns to reach its energy minimum when one monolayer is shifted relative to the other along any of six specific vectors, namely $\pm\frac{1}{3}\boldsymbol{a}$, $\pm\frac{1}{3}\boldsymbol{b}$, or $\pm\frac{1}{3}(\boldsymbol{a}+\boldsymbol{b})$, where $\boldsymbol{a}=[100]$ and $\boldsymbol{b}=[010]$ [55]. Such interlayer sliding can be experimentally realized using in situ biasing Cs-corrected transmission electron microscopy (Cs-TEM) [56]. For any of these sliding directions, the spin-degenerate Fermi surface is lifted. This occurs because each sliding configuration preserves only a single vertical mirror symmetry, while all other symmetries except the identity operation are broken. Moreover, the resulting pattern of spin splitting depends sensitively on the sliding direction, which is confined to the corresponding preserved mirror plane (see the outer parts in Fig. 2). Since the intrinsic T-odd SHC and SNC are directly linked to the pattern of spin splitting [35], interlayer sliding provides an effective means of modulating these spin responses.

Prior to calculating the SHC and SNC, we analyze the symmetry constraints on their in-plane components, i.e., σ_{xy}^{s} and α_{xy}^{s}, since the out-of-plane components are irrelevant in 2D systems. Because the SHC and SNC share identical symmetry constraints, we focus on the SHC here, and consider both the T-odd and T-even contributions for completeness. In the nonrelativistic limit, the symmetry constraints on the SHC can be determined using spin group theory. In this case, all collinear magnets possess an additional symmetry operation $[\bar{C}_2||T]$ [15, 16], which imposes $[\bar{C}_2||T]\sigma_{xy}^{s,\text{even}}=-\sigma_{xy}^{s,\text{even}}$, thereby forcing the T-even SHC to vanish regardless of whether sliding is present or not. In the absence of interlayer sliding, the T-odd SHC $\sigma_{xy}^{s,\text{odd}}$ also vanishes due to the constraint imposed by the $[C_2||M_z]$ symmetry, that is, $[C_2||M_z]\sigma_{xy}^{s,\text{odd}}=-\sigma_{xy}^{s,\text{odd}}$. Under interlayer sliding along the $\pm\frac{1}{3}\boldsymbol{a}$, $\pm\frac{1}{3}\boldsymbol{b}$, or $\pm\frac{1}{3}(\boldsymbol{a}+\boldsymbol{b})$ directions, however, only symmetry operations $[C_2||M_{[120]}]$, $[C_2||M_{[210]}]$, or $[C_2||M_{[1\bar{1}0]}]$ remains, respectively. These operations impose no constraints on $\sigma_{xy}^{s,\text{odd}}$, and thus a finite T-odd SHC becomes allowed in the sliding configurations.

When SOC is taken into account, the magnetic point group must be used, as the spin and crystal degrees of freedom become coupled. For convenience, we define the

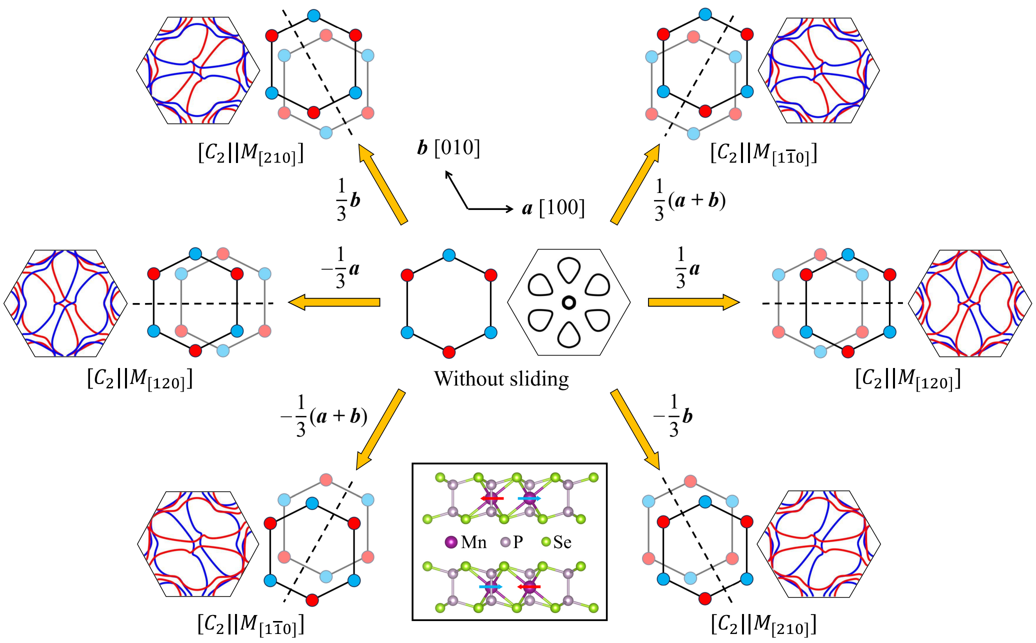

Fig. 2 Schematic illustrations of the magnetic structures and Fermi surface with and without interlayer sliding. The orange arrows mark the sliding directions, and the dashed lines indicate the preserved mirror planes. Red and blue spheres represent Mn atoms with opposite spin orientations, while the red and blue lines denote the Fermi surfaces associated with opposite spin polarizations, calculated at the Fermi energy $\varepsilon_F = -0.16$ eV. The symmetry operations remaining after each sliding configuration are listed below the corresponding schematic magnetic structure and its Fermi surface. The rectangular box highlights the atomic and magnetic structures of bilayer MnPSe$_3$ without sliding, where the red and blue arrows indicate the directions of the Mn spin moments.

Néel vector as $\boldsymbol{N} = \boldsymbol{S}_1 - \boldsymbol{S}_2$, where $\boldsymbol{S}_1$ and $\boldsymbol{S}_2$ denote the antiparallel spin moments within a unit cell. When $\boldsymbol{N}$ is parallel to the [100] direction (x axis), the non-sliding magnetic structure belongs to the magnetic point group $mm2.1$ (No. 7.1.20). In this group, the mirror symmetry M_z imposes the constraint $M_z\sigma_{xy}^{x(y)} = -\sigma_{xy}^{x(y)}$, indicating $\sigma_{xy}^{x(y)} = 0$, while allowing a finite σ_{xy}^{z} for both the T-odd and T-even components. For sliding along $\pm\frac{1}{3}\boldsymbol{a}$, the magnetic point group is reduced to $m.1$ (No. 4.1.9), where the vertical mirror $M_{[120]}$ enforces $M_{[120]}\sigma_{xy}^{y} = -\sigma_{xy}^{y}$, giving rise to $\sigma_{xy}^{y} = 0$, but permits finite σ_{xy}^{x} and σ_{xy}^{z} for both T-odd and T-even parts. In contrast, for sliding along $\pm\frac{1}{3}\boldsymbol{b}$ or $\pm\frac{1}{3}(\boldsymbol{a}+\boldsymbol{b})$, the magnetic point group further reduces to 1.1 (No. 1.1.1), where only the identity operation E remains. As a result, all in-plane SHC components become symmetry-allowed. The symmetry operations of the spin and magnetic point groups, together with their corresponding constraints on the SHC, are summarized in Tables 1 and 2, respectively.

For comparison, we also construct a bilayer MnPSe$_3$ with intralayer ferromagnetic order and interlayer antiferromagnetic order (see Fig. A1). The symmetry operations of the spin and magnetic point groups, together with their constraints on the SHC and SNC, are summarized in Tables A1 and A2, respectively, and discussed in detail in Appendix A. The results demonstrate that the specific type of in-plane magnetic order strongly constrains the SHC and SNC, highlighting the pivotal role of magnetic symmetry in tailoring spin transport properties.

To quantitatively evaluate the SHC and SNC using Eqs. (3), (4), and (8), the temperature $\mathcal{T}$ and spectral broadening parameter Γ must be specified. Given that monolayer MnPSe$_3$ has a Néel temperature exceeding 40 K and its bulk counterpart exhibits a Néel temperature of 68 K [57], we adopt a reasonable temperature of 50 K for the SHC and SNC calculations of bilayer MnPSe$_3$. According to deformation potential theory, bilayer MnPSe$_3$ possesses a high electron mobility of 418.6 cm^2·V^{-1}·s^{-1} in the valence band, which is considerably larger than the theoretical mobility of monolayer MoS$_2$ (72.2 cm^2·V^{-1}·s^{-1}) [58]. Based on Eq. (6), the corresponding relaxation time is estimated to be $\tau = 238.0$ fs, significantly longer than that of monolayer CrI$_3$ (30–70 fs) [59] and NiI$_2$ (22.7 fs) [36], indicating weak carrier scattering in bilayer MnPSe$_3$. The associated spectral broadening is then determined to be $\hbar\Gamma = 2.8$ meV.

The magnitude and sign of the nonrelativistic T-odd spin transport can be effectively modulated by interlayer sliding. Here, we take the spin Hall response with spin polarization along the x direction, $\sigma_{xy}^{x,\text{odd}}$, as an illustrative example, as shown in the top row of Fig. 3, while the

Table 1 Symmetry operations of bilayer MnPSe$_3$ under various slidings for spin point group (without SOC) and magnetic point group (with SOC).

	w/o SOC	
Non-sliding	$[E\Vert E]$	$[C_2\Vert M_z]$
	$[E\Vert C_{3z}^{\pm}]$	$[C_2\Vert PC_{6z}^{\pm}]$
	$[E\Vert C_{2[100]}]$	$[C_2\Vert M_{[210]}]$
	$[E\Vert C_{2[110]}]$	$[C_2\Vert M_{[120]}]$
	$[E\Vert C_{2[010]}]$	$[C_2\Vert M_{[1\bar{1}0]}]$
$\pm\frac{1}{3}\boldsymbol{a}$	$[E\Vert E]$	$[C_2\Vert M_{[120]}]$
$\pm\frac{1}{3}\boldsymbol{b}$	$[E\Vert E]$	$[C_2\Vert M_{[210]}]$
$\pm\frac{1}{3}(\boldsymbol{a}+\boldsymbol{b})$	$[E\Vert E]$	$[C_2\Vert M_{[1\bar{1}0]}]$
	w SOC ($\boldsymbol{N}\Vert x$-axis)	
Non-sliding	$E,\ C_{2[100]},\ M_z,\ M_{[120]}$	
$\pm\frac{1}{3}\boldsymbol{a}$	$E,\ M_{[120]}$	
$\pm\frac{1}{3}\boldsymbol{b}$	E	
$\pm\frac{1}{3}(\boldsymbol{a}+\boldsymbol{b})$	E	

Table 2 Symmetry constraints on the SHC components $\sigma_{xy}^{s,\text{odd/even}}$ imposed by the spin point group (without SOC) and the magnetic point group (with SOC). The corresponding constraints for the SNC are identical to those for the SHC.

	w/o SOC					
	$\sigma_{xy}^{x,\text{odd}}$	$\sigma_{xy}^{y,\text{odd}}$	$\sigma_{xy}^{z,\text{odd}}$	$\sigma_{xy}^{x,\text{even}}$	$\sigma_{xy}^{y,\text{even}}$	$\sigma_{xy}^{z,\text{even}}$
Non-sliding	✘	✘	✘	✘	✘	✘
$\pm\frac{1}{3}\boldsymbol{a}$	✔	✔	✔	✘	✘	✘
$\pm\frac{1}{3}\boldsymbol{b}$	✔	✔	✔	✘	✘	✘
$\pm\frac{1}{3}(\boldsymbol{a}+\boldsymbol{b})$	✔	✔	✔	✘	✘	✘
	w SOC ($\boldsymbol{N}\Vert x$-axis)					
	$\sigma_{xy}^{x,\text{odd}}$	$\sigma_{xy}^{y,\text{odd}}$	$\sigma_{xy}^{z,\text{odd}}$	$\sigma_{xy}^{x,\text{even}}$	$\sigma_{xy}^{y,\text{even}}$	$\sigma_{xy}^{z,\text{even}}$
Non-sliding	✘	✘	✔	✘	✘	✔
$\pm\frac{1}{3}\boldsymbol{a}$	✔	✘	✔	✔	✘	✔
$\pm\frac{1}{3}\boldsymbol{b}$	✔	✔	✔	✔	✔	✔
$\pm\frac{1}{3}(\boldsymbol{a}+\boldsymbol{b})$	✔	✔	✔	✔	✔	✔

cases with spin polarization along the y and z directions ($\sigma_{xy}^{y/z,\text{odd}}$) exhibit similar behavior. We analyze the interlayer sliding with the sequence of $\frac{1}{3}\boldsymbol{a} \to \frac{1}{3}(\boldsymbol{a}+\boldsymbol{b}) \to \frac{1}{3}\boldsymbol{b} \to -\frac{1}{3}\boldsymbol{a} \to -\frac{1}{3}(\boldsymbol{a}+\boldsymbol{b}) \to -\frac{1}{3}\boldsymbol{b}$, which proceeds counterclockwise in 60° intervals (see Fig. 2). For all sliding configurations, $\sigma_{xy}^{x,\text{odd}}$ is dominated by the intraband contribution, whereas the interband part is negligible. For the $\frac{1}{3}\boldsymbol{a}$ sliding, as the Fermi level ε_F moves downward from the valence-band maximum, $\sigma_{xy}^{x,\text{odd-intra}}$ develops a deep valley of $-12.3\ \mathrm{e}/4\pi$ at -0.16 eV and a peak of $11.6\ \mathrm{e}/4\pi$ at -0.24 eV. For the $\frac{1}{3}(\boldsymbol{a}+\boldsymbol{b})$ sliding, $\sigma_{xy}^{x,\text{odd-intra}}$ exhibits similar behavior but with reduced magnitudes, with the extrema decreased to $-6.3\ \mathrm{e}/4\pi$ and $5.7\ \mathrm{e}/4\pi$, respectively. In contrast, for the $\frac{1}{3}\boldsymbol{b}$ sliding, $\sigma_{xy}^{x,\text{odd-intra}}$ is exactly opposite in sign to that of the $\frac{1}{3}(\boldsymbol{a}+\boldsymbol{b})$ case. This sign reversal arises because the two corresponding crystal structures are related by the symmetry operation $[E\Vert M_{[100]}]$, which flips the sign of $\sigma_{xy}^{x,\text{odd-intra}}$. Furthermore, for the $-\frac{1}{3}\boldsymbol{a}$, $-\frac{1}{3}\boldsymbol{b}$, and $-\frac{1}{3}(\boldsymbol{a}+\boldsymbol{b})$ slidings (i.e., the opposite displacements of $\frac{1}{3}\boldsymbol{a}$, $\frac{1}{3}\boldsymbol{b}$, and $\frac{1}{3}(\boldsymbol{a}+\boldsymbol{b})$, respectively), $\sigma_{xy}^{x,\text{odd-intra}}$ retains the same magnitude but acquires the opposite sign compared with their positive-sliding counterparts. This behavior is enforced by the symmetry operation $[C_2\Vert M_z]$, which connects each pair of opposite sliding configurations.

To elucidate the microscopic origin of the variation in nonrelativistic T-odd spin transport under different sliding configurations, we examine its momentum-space distribution by calculating $D_{xy}^{x,\text{odd-intra}}$, as shown in the inset of the top row of Fig. 3. For the $\frac{1}{3}\boldsymbol{a}$ sliding, $D_{xy}^{x,\text{odd-intra}}$ spreads almost uniformly along the Fermi surface, indicating that $\sigma_{xy}^{x,\text{odd-intra}}$ arises predominantly from Fermi-surface contributions. More specifically, the spin-up and spin-down Fermi surfaces contribute nearly equally. The distribution of $D_{xy}^{x,\text{odd-intra}}$ is symmetric with respect to both the k_x and k_y axes due to the symmetry constraints $[C_2\Vert M_{[120]}]D_{xy}^{x,\text{odd-intra}}(k_x,k_y) = D_{xy}^{x,\text{odd-intra}}(k_x,-k_y)$ and $[C_2\Vert T][C_2\Vert M_{[120]}]D_{xy}^{x,\text{odd-intra}}(k_x,k_y) = D_{xy}^{x,\text{odd-intra}}(-k_x,k_y)$. The same symmetry analysis applies to the $-\frac{1}{3}\boldsymbol{a}$ sliding, however, in this case the sign of $D_{xy}^{x,\text{odd-intra}}$ is reversed relative to the $\frac{1}{3}\boldsymbol{a}$ configuration. This originates from the opposite spin polarizations of the Fermi surfaces produced by the two opposite sliding directions (also refer to Fig. 2), which are related by the symmetry operation $[C_2\Vert M_z]$. This symmetry imposes the constraint $[C_2\Vert M_z]D_{xy}^{x,\text{odd-intra}}(k_x,k_y) = -D_{xy}^{x,\text{odd-intra}}(k_x,k_y)$, thereby enforcing an overall sign reversal of $\sigma_{xy}^{x,\text{odd-intra}}$. For the $\pm\frac{1}{3}(\boldsymbol{a}+\boldsymbol{b})$ and $\pm\frac{1}{3}\boldsymbol{b}$ slidings, the spin-up and spin-down Fermi surfaces remain symmetrically distributed with respect to the $[C_2\Vert M_{[1\bar{1}0]}]$ and $[C_2\Vert M_{[210]}]$ symmetry operations, respectively. However, the quantity $D_{xy}^{x,\text{odd-intra}}$ itself does not remain symmetric under these operations. As a result, the contributions from the two spin channels become unbalanced — and may even acquire opposite signs — which ultimately reduces the magnitude of $\sigma_{xy}^{x,\text{odd-intra}}$.

Having clarified the sliding dependence of the SHC, we now turn to the SNC. As shown in the bottom row of Fig. 3, the SNC is likewise dominated by the T-odd intraband contribution, and its dependence on the sliding direction closely resembles that of the SHC, as both responses obey the same symmetry constraints. However, their energy-dependent behaviors differ markedly. At $\varepsilon_F = -0.16$ eV, where the T-odd intraband

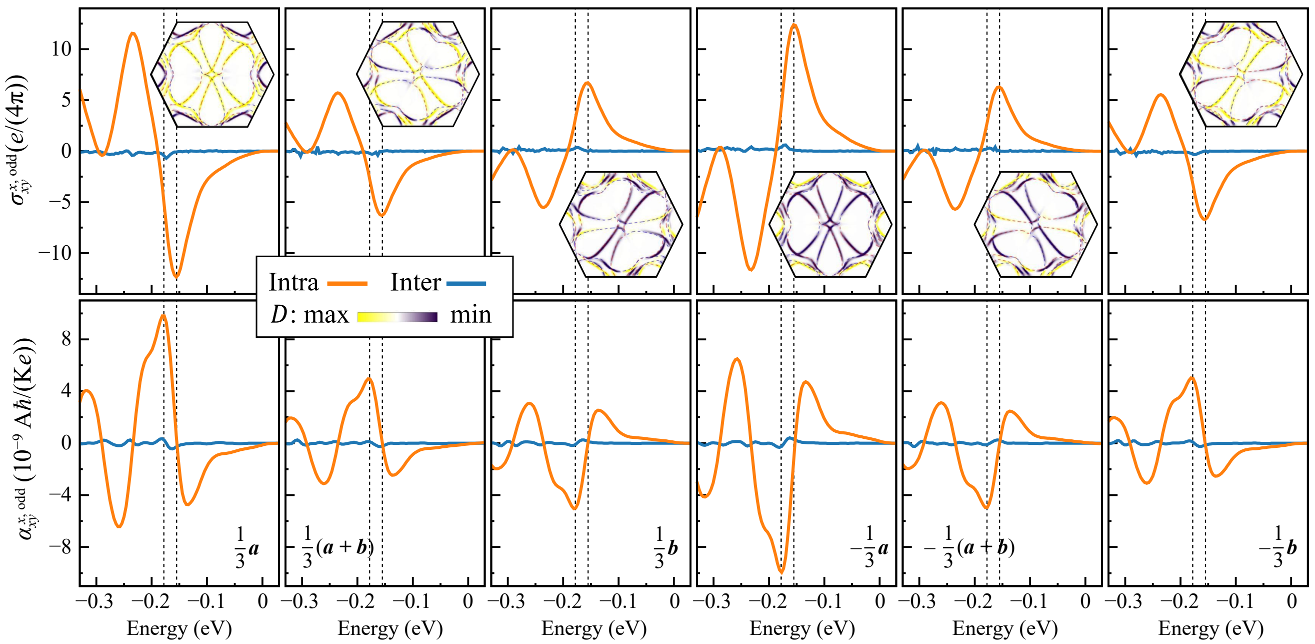

Fig. 3 The $\mathcal{T}$-odd SHC (top row) and SNC (bottom row) of bilayer MnPSe$_3$ for different interlayer-sliding configurations, calculated at 50 K without SOC. The two vertical black dashed lines mark the Fermi levels $\varepsilon_F = -0.16$ eV and -0.18 eV, respectively. The insets in the top row show the Fermi surfaces at $\varepsilon_F = -0.16$ eV, where the red and blue dashed lines denote opposite spin polarizations, together with the distribution of $D_{xy}^{x;\text{odd-intra}}(k_x, k_y)$ (color maps in arbitrary units).

SHC reaches an extremum, the corresponding SNC nearly vanishes. In contrast, at $\varepsilon_F = -0.18$ eV, the SNC attains a maximum value of 9.9×10^{-9}A$\hbar$/(Ke), coinciding with a region where the SHC exhibits a steep energy gradient. This correlation arises directly from the Mott relation,

$$\alpha_{xy}^{x} = -\frac{\pi^2}{3}\frac{k_B^2\mathcal{T}}{e}\left(\sigma_{xy}^{x}\right)', \tag{13}$$

which dictates that the SNC is proportional to the first-order energy derivative of the SHC.

When SOC is included, the T-even components of the SHC and SNC become symmetry-allowed. However, as shown in Fig. 4, their magnitudes remain negligible, so both responses continue to be dominated by the T-odd intraband contribution. The overall sliding and energy dependences of the SHC and SNC are thus qualitatively preserved in the presence of SOC, although their magnitudes undergo quantitative modifications. For the $\frac{1}{3}\boldsymbol{a}$ sliding, the first extremum of $\sigma_{xy}^{x,\text{odd-intra}}$ (located at $\varepsilon_F = -0.16$ eV) is reduced to $-6.0\ e/(4\pi)$, which corresponds to -1272.0 S$\hbar$/(cm$e$) when expressed in the conventional units of a three-dimensional system. Despite this decrease, the magnitude still exceeds those reported for non-collinear antiferromagnets Mn$_3X$ ($X =$ Sn, Ge, Ga), which exhibit values around 219 S$\hbar$/(cm$e$) [60], as well as nonmagnetic Ni$_{70}$Cu$_{30}$ (1136 S$\hbar$/(cm$e$)) [61] and nonmagnetic ZrXY ($X =$ Si, Ge; $Y =$ S, Se, Te), which reach approximately 755 S$\hbar$/(cm$e$) [62]. Similarly, the extremum of $\alpha_{xy}^{x,\text{odd-intra}}$ (at $\varepsilon_F = -0.19$ eV) decreases to 5.3×10^{-9} A$\hbar$/(Ke) (corresponded to 5.2 A$\hbar$/(Kme) in the unit of three-dimensional system). This value still surpasses those reported for nonmagnetic Ni$_{70}$Cu$_{30}$ (3.5 A$\hbar$/(Kme)) [61] and nonmagnetic ZrSiS (1.5 A$\hbar$/(Kme)) [62].

Figures 5(a) and 5(b) show the angular dependence of the T-odd intraband SHC and SNC with respect to the sliding direction. In the nonrelativistic limit, both quantities exhibit a clear 2π-periodic variation with the sliding angle β, defined as the angle between the sliding vector and $\frac{1}{3}\boldsymbol{a}$. The SHC and SNC reach their extrema for the $\pm\frac{1}{3}\boldsymbol{a}$ slidings and vanish when the sliding occurs along the y axis. The results reveal a pronounced anisotropy in the sliding-induced SHC and SNC, demonstrating that both the magnitude and sign of the spin transport can be tuned continuously by adjusting the sliding direction. This control is intrinsic to the sliding degree of freedom and is independent of the applied electric field or temperature gradient, providing a new mechanism for tuning spin currents in 2D altermagnets. When SOC is included, the SHC and SNC retain the same 2π periodicity and phase positions. However, their magnitudes are reduced compared with the nonrelativistic case, indicating that SOC partially suppresses the spin-transport response while preserving the overall angular anisotropy.

Finally, we evaluate the longitudinal electronic conductivity σ_{xx} and the charge-to-spin conversion efficiency $|\mathrm{CSE}|$, which quantify, respectively, the ability of an applied electric field to drive a longitudinal charge current and the efficiency with which that longitudinal

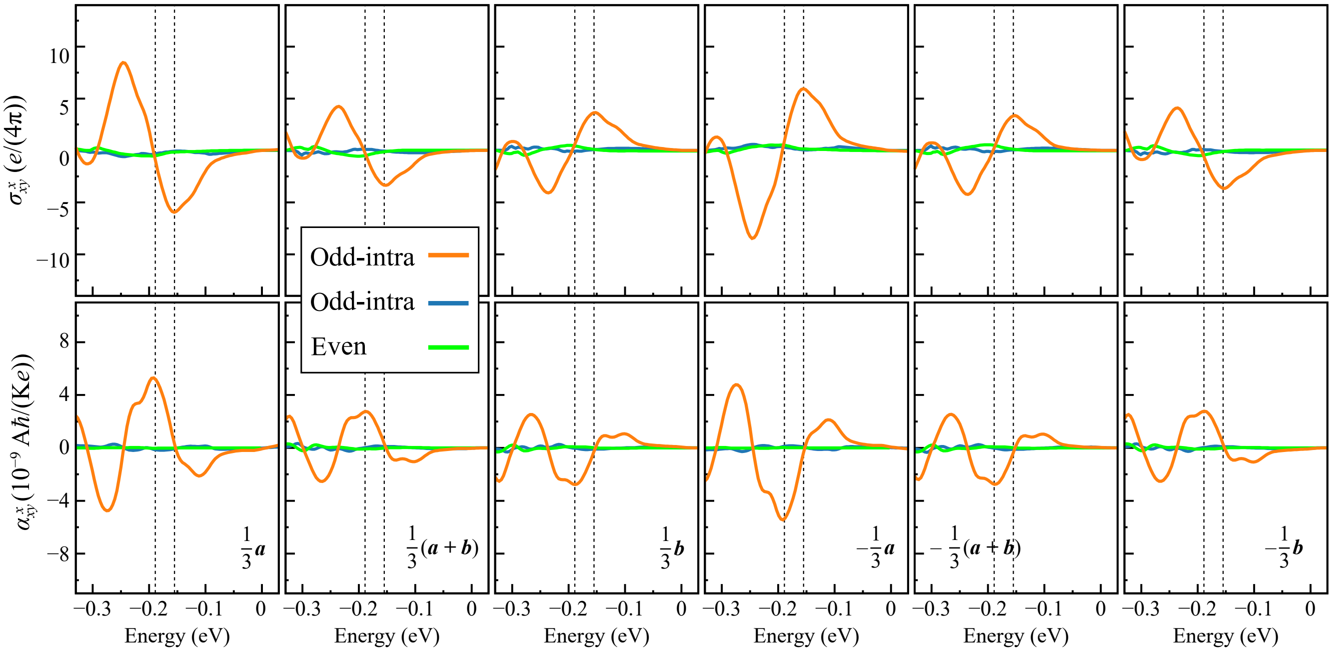

Fig. 4 The SHC (top row) and SNC (bottom row) of bilayer MnPSe$_3$ for different interlayer-sliding configurations, calculated at 50 K with SOC. The two vertical black dashed lines mark the Fermi levels $\varepsilon_F = -0.16$ eV and -0.19 eV, respectively.

charge current is converted into a transverse spin current. Specifically, the conversion efficiencies are defined as $|\mathrm{CSE}|^{\mathrm{SHE}} = |\sigma_{xy}^{s}/\sigma_{xx}| \times 100\%$ and $|\mathrm{CSE}|^{\mathrm{SNE}} = |\alpha_{xy}^{s}/\sigma_{xx}| \times 100\%$. As shown in Figs. 6(a) and (b), the values of $|\sigma_{xx}|$ are identical for the $\pm\frac{1}{3}\boldsymbol{a}$, $\pm\frac{1}{3}\boldsymbol{b}$, and $\pm\frac{1}{3}(\boldsymbol{a}+\boldsymbol{b})$ sliding configurations. This equivalence arises because each pair of opposite sliding configurations is related by the symmetry operation $[C_2||M_z]$ in the absence of SOC (or by M_z when SOC is included), which preserves $|\sigma_{xx}|$. Moreover, the $\pm\frac{1}{3}\boldsymbol{b}$ and $\pm\frac{1}{3}(\boldsymbol{a}+\boldsymbol{b})$ slidings also yield identical $|\sigma_{xx}|$, as they are connected by the symmetry operation $[E||M_{[100]}]$ without SOC (or by $M_{[100]}$ with SOC), which likewise preserves $|\sigma_{xx}|$. Below the valence-band maximum, $|\sigma_{xx}|$ increases monotonically with decreasing energy. For the $\pm\frac{1}{3}\boldsymbol{a}$ slidings, a pronounced peak of approximately $3.9 \times 10^{4}\ e^2/h$ appears at $\varepsilon_F = -0.19$ eV, whereas this peak shifts to $\varepsilon_F = -0.22$ eV for the $\pm\frac{1}{3}\boldsymbol{b}$ and $\pm\frac{1}{3}(\boldsymbol{a}+\boldsymbol{b})$ slidings. Upon including SOC, the overall magnitude of $|\sigma_{xx}|$ is slightly reduced, indicating that SOC weakly suppresses the longitudinal charge transport.

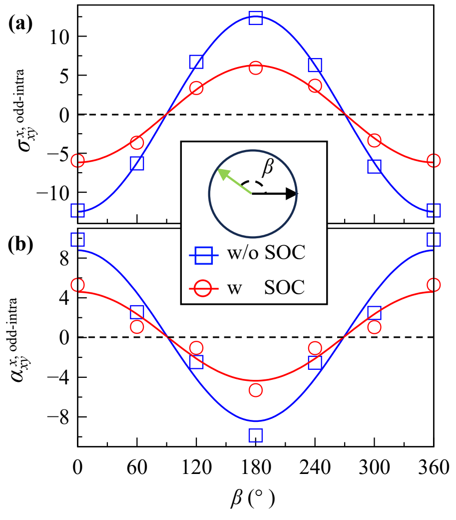

Fig. 5 **(a)** The SHC (evaluated at $\varepsilon_F = -0.16$ eV, without and with SOC) and **(b)** the SNC (evaluated at $\varepsilon_F = -0.18$ eV without SOC and $\varepsilon_F = -0.19$ eV with SOC) as a function of the orientation of the sliding vector. The green arrow indicates the orientation angle β, measured from the black arrow representing the $\frac{1}{3}\boldsymbol{a}$ sliding direction. The quantities in (a) and (b) are given in units of $e/4\pi$ and $10^{-9}\mathrm{A}\hbar/(\mathrm{K}e)$, respectively.

The energy-dependent $|\mathrm{CSE}|$ for different sliding configurations is shown in Figs. 6(c)–(f). In the absence of SOC, both $|\mathrm{CSE}|^{\mathrm{SHE}}$ and $|\mathrm{CSE}|^{\mathrm{SNE}}$ exhibit pronounced oscillations with multiple peaks below $\varepsilon_F = 0$ eV, reflecting their strong sensitivity to hole doping. The maximum values reach approximately $12.5\ (\hbar/e)\%$ for $|\mathrm{CSE}|^{\mathrm{SHE}}$ and $7.5 \times 10^{5}\ (\mathrm{A}\hbar/(\mathrm{SK}e))\%$ for $|\mathrm{CSE}|^{\mathrm{SNE}}$. Upon inclusion of SOC, the overall magnitudes are moderately reduced, and the peak structures become slightly smoother. This suppression indicates that SOC partially diminishes the charge-to-spin conversion process. Since σ_{xx} is also reduced when SOC is included, the decrease in both $|\mathrm{CSE}|^{\mathrm{SHE}}$ and $|\mathrm{CSE}|^{\mathrm{SNE}}$ can be reasonably attributed to the concomitant reduction in the SHC and SNC. Despite this overall reduction, the energy dependence of $|\mathrm{CSE}|$ still faithfully reflects the intrinsic nature of the charge-to-spin conversion mediated by interlayer sliding.

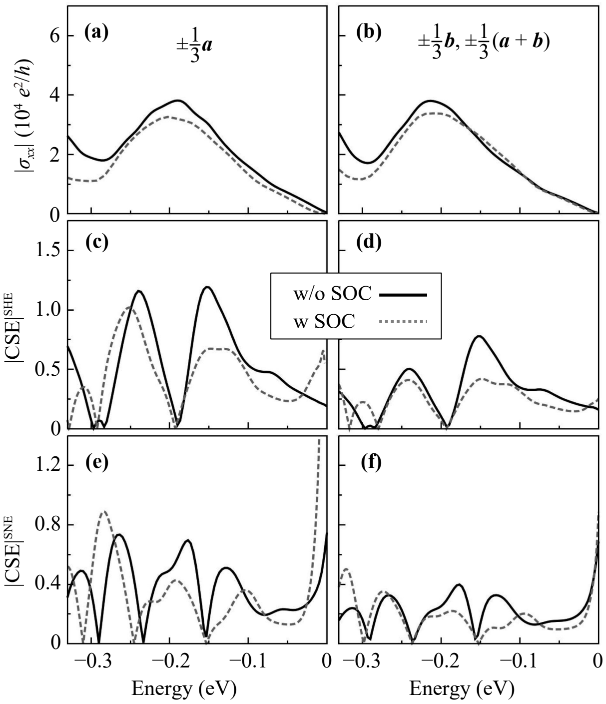

Fig. 6 **(a, b)** The longitudinal conductivity $|\sigma_{xx}|$, **(c, d)** the charge–spin conversion efficiency in the SHE, $|\mathrm{CSE}|^{\mathrm{SHE}}$, and **(e, f)** the corresponding efficiency in the SNE, $|\mathrm{CSE}|^{\mathrm{SNE}}$, calculated for different sliding configurations. The quantities in panels (c, d) and (e, f) are given in units of $10\,(\hbar/e)\%$ and $10^6\,(\mathrm{A}\hbar/(\mathrm{SK}e))\%$, respectively.

4 Summary

In summary, by combining group-theory analysis and first-principles calculations, we have investigated the SHE and SNE in the 2D bilayer altermagnet MnPSe$_3$. In the nonrelativistic limit, spin-group analysis reveals that interlayer sliding induces d-wave — like spin splittings, which give rise to nonvanishing spin Hall and spin Nernst responses. We shown that both the SHE and SNE are dominated by the T-odd intraband contribution. When the sliding direction changes, the associated symmetry operation is modified, leading to corresponding changes in the spin splitting of the Fermi surface and, consequently, to a tunable modulation of the spin-transport properties. This modulation originates from symmetry-induced variations in the opposite spin polarizations of the band structures generated by different directions of interlayer sliding. In addition, interlayer sliding can efficiently modulate the charge-to-spin conversion efficiency. When SOC is included, the proposed mechanism remains valid. Specifically, under the $\frac{1}{3}\boldsymbol{a}$ sliding, the SHC and SNC reach large values of $-6.0\,e/4\pi$ at $\varepsilon_F=-0.16$ eV and 5.3×10^{-9} A$\hbar$/(Ke) at $\varepsilon_F=-0.19$ eV, respectively. Our findings establish interlayer sliding as an effective route to control the patterns of band spin-splitting as well as the spin Hall and Nernst transport in 2D layered altermagnets, paving the way for advancements in altermagnetic spintronics and spin-caloritronics.

Declarations The authors declare that they have no competing interests and there are no conflicts.

Acknowledgments This work was supported by the National Natural Science Foundation of China (Grant Nos. W2511003, 12274027, and 12274028) and the National Key R&D Program of China (Grant Nos. 2022YFA1402600 and 2022YFA1403800). Additional support is provided by the Teaching Research Project of Physics Major in Higher Education Institutions, Ministry of Education of China (Grant No. JZW-24-JW-01), and by the Project of the Beijing Higher Education Society (Grant No. MS2024299). Y.M. acknowledges support by the Deutsche Forschungsgemeinschaft TRR 173/3-268565370 (Project A11) and TRR 288/2-422213477 (Project B06).

Appendix A: Bilayer MnPSe$_3$ with intralayer ferromagnetic order and interlayer antiferromagnetic order

Figure A1 shows the atomic and magnetic structures of non-sliding bilayer MnPSe$_3$ with intralayer ferromagnetic order and interlayer antiferromagnetic order. In the absence of SOC, the T-even SHC has to vanish due to the additional symmetry operation $[\bar{C}_2||T]$ arising from the collinear magnetic order. Without sliding, the crystallographic point group is $\mathbb{G}=D_{3h}$. Using its halving subgroup $\mathbb{H}=C_{3v}$, the spin point group is generated: $[E||E]$, $[E||C_{3z}^{\pm}]$, $[E||M_\alpha]$ with $\alpha=[120],[1\bar{1}0],[210]$, $[C_2||M_z]$, $[C_2||PC_{6z}^{\pm}]$, and $[C_2||C_{2\alpha}]$ with $\alpha=[100],[110],[010]$. The T-odd SHC vanishes due to the constraint imposed by $[C_2||M_z]$. With sliding along the $\pm\frac{1}{3}\boldsymbol{a}$ direction, the spin point group changes to: $[E||E]$ and $[E||M_{[120]}]$, where $[E||M_{[120]}]\sigma_{xy}^{s,\mathrm{odd}}=-\sigma_{xy}^{s,\mathrm{odd}}$, forcing the T-odd SHC to be zero. In contrast, with sliding along the $\pm\frac{1}{3}\boldsymbol{b}$ $(\pm\frac{1}{3}(\boldsymbol{a}+\boldsymbol{b}))$ direction, the spin point group becomes $[E||E]$ and $[E||M_{[210]}]$ ($[E||E]$ and $[E||M_{[1\bar{1}0]}]$), imposing no constraints on $\sigma_{xy}^{s,\mathrm{odd}}$, and hence a finite T-odd SHC is expected.

When SOC is taken into account, the non-sliding configuration $(\boldsymbol{N}\parallel x-\text{axis})$ belongs to the magnetic

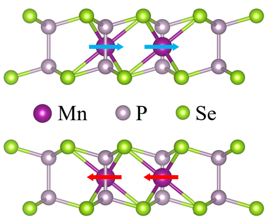

Fig. A1 The atomic and magnetic structures of non-sliding bilayer MnPSe$_3$ with intralayer ferromagnetic order and interlayer antiferromagnetic order. The red and blue arrows indicate the directions of the Mn spin moments.

Table A1 Symmetry operations of spin point group (without SOC) and magnetic point group (with SOC) for non-sliding and sliding bilayer MnPSe₃ with intralayer ferromagnetic order and interlayer antiferromagnetic order.

	w/o SOC	
Non-sliding	$[E\|E]$ $[E\|C_{3z}^{\pm}]$ $[E\|M_{[120]}]$ $[E\|M_{[1\bar{1}0]}]$ $[E\|M_{[210]}]$	$[C_2\|M_z]$ $[C_2\|PC_{6z}^{\pm}]$ $[C_2\|C_{2[100]}]$ $[C_2\|C_{2[110]}]$ $[C_2\|C_{2[010]}]$
$\pm\frac{1}{3}\boldsymbol{a}$	$[E\|E]$	$[E\|M_{[120]}]$
$\pm\frac{1}{3}\boldsymbol{b}$	$[E\|E]$	$[E\|M_{[210]}]$
$\pm\frac{1}{3}(\boldsymbol{a}+\boldsymbol{b})$	$[E\|E]$	$[E\|M_{[1\bar{1}0]}]$
	w SOC ($\boldsymbol{N}\|x$-axis)	
Non-sliding	$E,\ C_{2[100]}T,\ M_z,\ M_{[120]}T$	
$\pm\frac{1}{3}\boldsymbol{a}$	$E,\ M_{[120]}T$	
$\pm\frac{1}{3}\boldsymbol{b}$	E	
$\pm\frac{1}{3}(\boldsymbol{a}+\boldsymbol{b})$	E	

point group $m'm2'$ (No. 7.3.22). In this group, the mirror symmetry M_z imposes the constraint $M_z\sigma_{xy}^{x(y)} = -\sigma_{xy}^{x(y)}$, and $M_{[120]}T$ imposes the constraint $M_{[120]}T\sigma_{xy}^{z,\text{odd}} = -\sigma_{xy}^{z,\text{odd}}$. These two constraints force $\sigma_{xy}^{x(y)}$ and $\sigma_{xy}^{z,\text{odd}}$ to be zero, respectively, while a finite $\sigma_{xy}^{z,\text{even}}$ is allowed. When sliding is introduced along the $\pm\frac{1}{3}\boldsymbol{a}$ direction, the magnetic point group is reduced to m' (No. 4.3.11). Here, the symmetry operation $M_{[120]}T$ enforces $M_{[120]}T\sigma_{xy}^{x(z),\text{odd}} = -\sigma_{xy}^{x(z),\text{odd}}$ and $M_{[120]}T\sigma_{xy}^{y,\text{even}} = -\sigma_{xy}^{y,\text{even}}$, giving rise to $\sigma_{xy}^{x(z),\text{odd}} = 0$ and $\sigma_{xy}^{y,\text{even}} = 0$, respectively, whereas finite values are permitted for the components $\sigma_{xy}^{y,\text{odd}}$ and $\sigma_{xy}^{x(z),\text{even}}$. For slidings along the $\pm\frac{1}{3}\boldsymbol{b}$ or $\pm\frac{1}{3}(\boldsymbol{a}+\boldsymbol{b})$, the magnetic point group is further reduced to 1.1 (No. 1.1.1), where only the identity operation E remains. Consequently, all SHC components become symmetry-allowed. In summary, the symmetry operations of the spin and magnetic point groups, together with their constraints on the SHC, are collected in Tables A1 and A2, respectively.

Table A2 Symmetry constraints on the SHC $\sigma_{xy}^{s,\text{odd/even}}$ imposed by the spin point group (without SOC) and the magnetic point group (with SOC) for non-sliding and sliding bilayer MnPSe₃ with intralayer ferromagnetic order and interlayer antiferromagnetic order. The corresponding constraints for the SNC are identical to those for the SHC.

	w/o SOC					
	$\sigma_{xy}^{x,\text{odd}}$	$\sigma_{xy}^{y,\text{odd}}$	$\sigma_{xy}^{z,\text{odd}}$	$\sigma_{xy}^{x,\text{even}}$	$\sigma_{xy}^{y,\text{even}}$	$\sigma_{xy}^{z,\text{even}}$
Non-sliding	✘	✘	✘	✘	✘	✘
$\pm\frac{1}{3}\boldsymbol{a}$	✘	✘	✘	✘	✘	✘
$\pm\frac{1}{3}\boldsymbol{b}$	✔	✔	✔	✘	✘	✘
$\pm\frac{1}{3}(\boldsymbol{a}+\boldsymbol{b})$	✔	✔	✔	✘	✘	✘
	w SOC ($\boldsymbol{N}\|x$-axis)					
	$\sigma_{xy}^{x,\text{odd}}$	$\sigma_{xy}^{y,\text{odd}}$	$\sigma_{xy}^{z,\text{odd}}$	$\sigma_{xy}^{x,\text{even}}$	$\sigma_{xy}^{y,\text{even}}$	$\sigma_{xy}^{z,\text{even}}$
non-sliding	✘	✘	✘	✘	✘	✔
$\pm\frac{1}{3}\boldsymbol{a}$	✘	✔	✘	✔	✘	✔
$\pm\frac{1}{3}\boldsymbol{b}$	✔	✔	✔	✔	✔	✔
$\pm\frac{1}{3}(\boldsymbol{a}+\boldsymbol{b})$	✔	✔	✔	✔	✔	✔

References

1. T. Jungwirth, J. Wunderlich, and K. Olejnık, Spin Hall effect devices, *Nat. Mater.* 11(5), 382 (2012)
2. J. Sinova, S. O. Valenzuela, J. Wunderlich, C. H. Back, and T. Jungwirth, Spin Hall effects, *Rev. Mod. Phys.* 87(4), 1213 (2015)
3. J. Smit, The spontaneous Hall effect in ferromagnetics I, *Physica* 21(6–10), 877 (1955)
4. J. Smit, The spontaneous Hall effect in ferromagnetics II, *Physica* 24(1–5), 39 (1958)
5. S. Murakami, N. Nagaosa, and S. C. Zhang, Dissipationless quantum spin current at room temperature, *Science* 301(5638), 1348 (2003)
6. J. Sinova, D. Culcer, Q. Niu, N. A. Sinitsyn, T. Jungwirth, and A. H. MacDonald, Universal intrinsic spin Hall effect, *Phys. Rev. Lett.* 92(12), 126603 (2004)
7. A. Mook, R. R. Neumann, A. Johansson, J. Henk, and I. Mertig, Origin of the magnetic spin Hall effect: Spin current vorticity in the Fermi sea, *Phys. Rev. Res.* 2(2), 023065 (2020)
8. M. Kimata, H. Chen, K. Kondou, S. Sugimoto, P. K. Muduli, M. Ikhlas, Y. Omori, T. Tomita, A. H. MacDonald, S. Nakatsuji, and Y. Otani, Magnetic and magnetic inverse spin Hall effects in a non-collinear antiferromagnet, *Nature* 565(7741), 627 (2019)
9. X. Chen, S. Shi, G. Shi, X. Fan, C. Song, X. Zhou, H. Bai, L. Liao, Y. Zhou, H. Zhang, A. Li, Y. Chen, X. Han, S. Jiang, Z. Zhu, H. Wu, X. Wang, D. Xue, H. Yang, and F. Pan, Observation of the antiferromagnetic spin Hall effect, *Nat. Mater.* 20(6), 800 (2021)
10. W. Feng, Y. Yao, W. Zhu, J. Zhou, W. Yao, and D. Xiao, Intrinsic spin Hall effect in monolayers of group-VI dichalcogenides: A first-principles study, *Phys. Rev. B* 86(16), 165108 (2012)
11. G. Y. Guo, S. Murakami, T. W. Chen, and N. Nagaosa, Intrinsic spin Hall effect in platinum: First-principles calculations, *Phys. Rev. Lett.* 100(9), 096401 (2008)
12. E. Derunova, Y. Sun, C. Felser, S. S. P. Parkin, B. Yan, and M. N. Ali, Giant intrinsic spin Hall effect in W₃Ta and other A15 superconductors, *Sci. Adv.* 5(4), eaav8575 (2019)
13. H. Kontani, J. Goryo, and D. S. Hirashima, Intrinsic spin Hall effect in the s-wave superconducting state:

Analysis of the Rashba model, *Phys. Rev. Lett.* 102(8), 086602 (2009)

14. C. K. Safeer, J. Ingla-Aynés, F. Herling, J. H. Garcia, M. Vila, N. Ontoso, M. R. Calvo, S. Roche, L. E. Hueso, and F. Casanova, Room-temperature spin Hall effect in graphene/$\mathrm{MoS_2}$ van der Waals heterostructures, *Nano Lett.* 19(2), 1074 (2019)
15. L. Šmejkal, J. Sinova, and T. Jungwirth, Beyond conventional ferromagnetism and antiferromagnetism: A phase with nonrelativistic spin and crystal rotation symmetry, *Phys. Rev. X* 12, 031042 (2022)
16. L. Šmejkal, J. Libor, and T. Jungwirth, Emerging research landscape of altermagnetism, *Phys. Rev. X* 12, 040501 (2022)
17. L. Bai, W. Feng, S. Liu, L. Šmejkal, Y. Mokrousov, and Y. Yao, Altermagnetism: Exploring new frontiers in magnetism and spintronics, *Adv. Funct. Mater.* 34(49), 2409327 (2024)
18. L. Šmejkal, R. González-Hernández, T. Jungwirth, and J. Sinova, Crystal time-reversal symmetry breaking and spontaneous Hall effect in collinear antiferromagnets, *Sci. Adv.* 6, eaaz8809 (2020)
19. X. Zhou, W. Feng, X. Yang, G. Y. Guo, and Y. Yao, Crystal chirality magneto-optical effects in collinear antiferromagnets, *Phys. Rev. B* 104(2), 024401 (2021)
20. J. A. Ouassou, A. Brataas, and J. Linder, dc Josephson effect in altermagnets, *Phys. Rev. Lett.* 131(7), 076003 (2023)
21. J. Krempasky, L. Šmejkal, S. W. D'Souza, M. Hajlaoui, G. Springholz, K. Uhlrova, F. Alarab, P. C. Constantinou, V. Strocov, D. Usanov, W. R. Pudelko, R. González-Hernández, A. Birk Hellenes, Z. Jansa, H. Reichlova, Z. Šoban, R. D. Gonzalez Betancourt, P. Wadley, J. Sinova, D. Kriegner, J. Minár, J. H. Dil, and T. Jungwirth, Altermagnetic lifting of Kramers spin degeneracy, *Nature* 626, 517 (2024)
22. Z. Jin, Z. Zeng, Y. Cao, and P. Yan, Skyrmion Hall effect in altermagnets, *Phys. Rev. Lett.* 133(19), 196701 (2024)
23. Y. Fang, J. Cano, and S. A. A. Ghorashi, Quantum geometry induced nonlinear transport in altermagnets, *Phys. Rev. Lett.* 133(10), 106701 (2024)
24. R. W. Zhang, C. Cui, R. Li, J. Duan, L. Li, Z. M. Yu, and Y. Yao, Predictable gate-field control of spin in altermagnets with spin-layer coupling, *Phys. Rev. Lett.* 133(5), 056401 (2024)
25. X. Zhou, W. Feng, R. W. Zhang, L. Šmejkal, J. Sinova, Y. Mokrousov, and Y. Yao, Crystal thermal transport in altermagnetic $\mathrm{RuO_2}$, *Phys. Rev. Lett.* 132(5), 056701 (2024)
26. P. A. McClarty and J. G. Rau, Landau theory of altermagnetism, *Phys. Rev. Lett.* 132(17), 176702 (2024)
27. L. Šmejkal, A. Marmodoro, K. H. Ahn, R. González-Hernández, I. Turek, S. Mankovsky, H. Ebert, S. W. D' Souza, O. Šipr, J. Sinova, and T. Jungwirth, Chiral magnons in altermagnetic $\mathrm{RuO_2}$, *Phys. Rev. Lett.* 131, 256703 (2023)
28. S. A. A. Ghorashi, T. L. Hughes, and J. Cano, Altermagnetic routes to Majorana modes in zero net magnetization, *Phys. Rev. Lett.* 133(10), 106601 (2024)
29. T. Sato, S. Haddad, I. C. Fulga, F. F. Assaad, and J. van den Brink, Altermagnetic anomalous Hall effect emerging from electronic correlations, *Phys. Rev. Lett.* 133(8), 086503 (2024)
30. Z. Liu, M. Ozeki, S. Asai, S. Itoh, and T. Masuda, Chiral split magnon in altermagnetic MnTe, *Phys. Rev. Lett.* 133(15), 156702 (2024)
31. T. He, L. Li, C. Cui, R. W. Zhang, Z. M. Yu, G. Liu, and X. Zhang, Quasi-one-dimensional spin transport in altermagnetic Z_3 nodal net metals, *Phys. Rev. Lett.* 133(14), 146602 (2024)
32. L. Bai, R. W. Zhang, W. Feng, and Y. Yao, Anomalous Hall effect in type IV 2D collinear magnets, *Phys. Rev. Lett.* 135(3), 036702 (2025)
33. S. Liu, Z. Zhang, L. Bai, and W. Feng, Anomalous transport properties in the two-dimensional topological altermagnet $\mathrm{V_2Te_2O}$, *Phys. Rev. B* 111(18), 184437 (2025)
34. X. Wang, S. Liu, L. Bai, R. W. Zhang, Y. Yao, and W. Feng, Layer Hall and layer spin Hall effects in two-dimensional altermagnets induced by spin-layer coupling, *Phys. Rev. B* 112(13), 134421 (2025)
35. R. González-Hernández, L. Šmejkal, K. Výborný, Y. Yahagi, J. Sinova, T. Jungwirth, and J. Železný, Efficient electrical spin-splitter based on non-relativistic collinear antiferromagnetism, *Phys. Rev. Lett.* 126, 127701 (2021)
36. J. W. Gonzalez and L. Rosales, Strain-induced half-metallicity and giant Wiedemann–Franz violation in monolayer $\mathrm{NiI_2}$, arXiv: 2506.06855 (2025)
37. Z. Zhou, Y. L. Li, Z. G. Sun, J. F. Wang, and M. Y. Chen, The enhanced effect of magnetism on the thermoelectric performance of a $\mathrm{CrI_3}$ monolayer, *Nanoscale* 15(3), 1032 (2023)
38. M. Yu, W. Gao, X. Shi, Q. Yuan, B. Wang, L. Ju, and H. Yin, Polar iodate $\mathrm{BiO(IO_3)}$: A two-dimensional ultrawide-bandgap semiconductor with high carrier mobility and robust piezoelectricity, *Results Phys.* 59, 107561 (2024)
39. J. Qiao, X. Kong, Z. Hu, F. Yang, and W. Ji, High-mobility transport anisotropy and linear dichroism in few-layer black phosphorus, *Nat. Commun.* 5(1), 4475 (2014)
40. K. Behnia, Fundamentals of Thermoelectricity, Oxford University Press, 2015
41. H. Houten, L. W. Molenkamp, C. W. J. Beenakker, and C. T. Foxon, Thermo-electric properties of quantum point contacts, *Semicond. Sci. Technol.* 7(3B), B215 (1992)
42. N. W. Ashcroft and N. D. Mermin, Solid State Physics, Harcourt College, 1976
43. G. Grosso and G. P. Parravicini, Solid State Physics, Academic Press, 2000
44. T. J. Scheidemantel, C. Ambrosch-Draxl, T. Thonhauser, J. V. Badding, and J. O. Sofo, Transport coefficients from first-principles calculations, *Phys. Rev. B* 68(12), 125210 (2003)
45. G. Pizzi, D. Volja, B. Kozinsky, M. Fornari, and N. Marzari, BoltzWann: A code for the evaluation of thermoelectric and electronic transport properties with a maximally-localized Wannier functions basis, *Comput. Phys. Commun.* 185(1), 422 (2014)
46. G. Kresse and J. Hafner, *Ab initio* molecular dynamics

for liquid metals, *Phys. Rev. B* 47(1), 558 (1993)

47. G. Kresse and J. Hafner, *Ab initio* molecular-dynamics simulation of the liquid-metal–amorphous-semiconductor transition in germanium, *Phys. Rev. B* 49(20), 14251 (1994)
48. J. P. Perdew, K. Burke, and M. Ernzerhof, Generalized gradient approximation made simple, *Phys. Rev. Lett.* 77(18), 3865 (1996)
49. G. Kresse and D. Joubert, From ultrasoft pseudopotentials to the projector augmented-wave method, *Phys. Rev. B* 59(3), 1758 (1999)
50. S. L. Dudarev, G. A. Botton, S. Y. Savrasov, C. J. Humphreys, and A. P. Sutton, Electron-energy-loss spectra and the structural stability of nickel oxide: An LSDA+U study, *Phys. Rev. B* 57(3), 1505 (1998)
51. S. Grimme, J. Antony, S. Ehrlich, and H. Krieg, A consistent and accurate *ab initio* parametrization of density functional dispersion correction (DFT-D) for the 94 elements H-Pu, *J. Chem. Phys.* 132(15), 154104 (2010)
52. G. Pizzi, V. Vitale, R. Arita, S. Blügel, F. Freimuth, G. Géranton, M. Gibertini, D. Gresch, C. Johnson, T. Koretsune, J. Ibañez-Azpiroz, H. Lee, J.M. Lihm, D. Marchand, A. Marrazzo, Y. Mokrousov, J. I. Mustafa, Y. Nohara, Y. Nomura, L. Paulatto, S. Poncé, T. Ponweiser, J. Qiao, F. Thöle, S. S. Tsirkin, M. Wierzbowska, N. Marzari, D. Vanderbilt, I. Souza, A. A. Mostofi, and J. R. Yates, Wannier90 as a community code: New features and applications, *J. Phys.: Condens. Matter* 32(16), 165902 (2020)
53. S. Lai, H. Liu, Z. Zhang, J. Zhao, X. Feng, N. Wang, C. Tang, Y. Liu, K. S. Novoselov, S. A. Yang, and W. Gao, Third-order nonlinear Hall effect induced by the Berry-connection polarizability tensor, *Nat. Nanotechnol.* 16(8), 869 (2021)
54. W. Sun, C. Yang, W. Wang, Y. Liu, X. Wang, S. Huang, and Z. Cheng, Proposing altermagnetic-ferroelectric type-III multiferroics with robust magnetoelectric coupling, *Adv. Mater.* 37(26), 2502575 (2025)
55. S. Sheoran and P. Dev, Spontaneous anomalous Hall effect in two-dimensional altermagnets, *Phys. Rev. B* 111(18), 184407 (2025)
56. F. Sui, H. Li, R. Qi, M. Jin, Z. Lv, M. Wu, X. Liu, Y. Zheng, B. Liu, R. Ge, Y. N. Wu, R. Huang, F. Yue, J. Chu, and C. Duan, Atomic-level polarization reversal in sliding ferroelectric semiconductors, *Nat. Commun.* 15(1), 3799 (2024)
57. Z. Ni, A. V. Haglund, H. Wang, B. Xu, C. Bernhard, D. G. Mandrus, X. Qian, E. J. Mele, C. L. Kane, and L. Wu, Imaging the Néel vector switching in the monolayer antiferromagnet $MnPSe_3$ with strain-controlled Ising order, *Nat. Nanotechnol.* 16(7), 782 (2021)
58. S. Bertolazzi, J. Brivio, and A. Kis, Stretching and Breaking of Ultrathin MoS_2, *ACS Nano* 5(12), 9703 (2011)
59. Z. Wu, J. Yu, and S. Yuan, Strain-tunable magnetic and electronic properties of monolayer CrI_3, *Phys. Chem. Chem. Phys.* 21(15), 7750 (2019)
60. G. Y. Guo and T. C. Wang, Large anomalous Nernst and spin Nernst effects in the noncollinear antiferromagnets Mn_3X (X = Sn, Ge, Ga), *Phys. Rev. B* 96(22), 224415 (2017)
61. W. Y. Li, C. H. Lin, G. Y. Guo, S. Y. Huang, and D. Qu, Large spin Nernst effect in the $Ni_{70}Cu_{30}$ alloy, *Phys. Rev. B* 111(5), 054421 (2025)
62. Y. Yen and G. Y. Guo, Tunable large spin Hall and spin Nernst effects in the Dirac semimetals ZrXY (X = Si, Ge; Y = S, Se, Te), *Phys. Rev. B* 101(6), 064430 (2020)